High Efficiency and Wide Bandwidth Quasi-Load Insensitive Class-E Operation Utilizing Package Integration

Qureshi, Abdul Raheem; Acar, Mustafa; Pires, Sergio C.; de Vreede, Leonardus Cornelis Nicolaas

DOI
10.1109/TMTT.2018.2868876

Publication date
2018

Document Version
Accepted author manuscript

Published in
IEEE Transactions on Microwave Theory and Techniques

High Efficiency and Wide Bandwidth Quasi-Load Insensitive Class-E Operation Utilizing Package Integration

Abdul Raheem Qureshi, *Student Member, IEEE*, Mustafa Acar, *Member, IEEE*, Sergio C. Pires, *Member, IEEE*, and Leonardus Cornelis Nicolaas de Vreede, *Senior Member, IEEE*

***Abstract*— Packaged integrated low-pass quasi-load insensitive (QLI) class-E matching is proposed for the realization of energy-efficient wideband Doherty and outphasing transmitters. In view of this, a dedicated QLI class-E harmonic matching technique, suitable for in-package integration has been developed, optimized, and evaluated. As proof of concept, very compact, as well as easy to assemble, dual-input load-modulating transmitters have been realized. In this paper, we focus on a QLI class-E matched wideband Doherty that provides 71% peak efficiency (±3%) at 48-dBm saturated output power and 49% (±7%) efficiency at 6-dB power backoff, over a 1200-MHz frequency span (1.4–2.6 GHz), yielding 60% fractional bandwidth (BW). When tested with single-carrier long-term evolution (LTE) signals, having a 7-dB peak-to-average ratio, average efficiency remains close to 49% (±3%) for the entire 60% fractional BW. The realized demonstrator shows excellent linearizability with adjacent channel power ratio and normalized mean square error levels below −50 dBc and −36 dB, respectively, even when operated in simultaneous dual-band LTE operation.**

***Index Terms*— Doherty, dual input, harmonic matching, high efficiency, package integration, quasi-load insensitive (QLI) class-E, wideband.**

I. Introduction

THERE is a growing demand for next-generation communication systems that can handle higher data rates in a more energy efficient manner. These systems should offer higher performance at reduced operational costs in current and future wireless networks. These tasks are especially challenging in the transmit path, where high average efficiency is required in the amplification of wideband or carrier aggregated complex modulated signals with high peak-to-average power ratios (PARs). To address these needs, over time, various Doherty power amplifiers (DPAs), and outphasing transmitters concepts have been investigated, since they can combine low-hardware complexity, with good average efficiency for moderate to large video bandwidths (BWs) [1]–[4]. In spite of numerous advancements in DPAs and outphasing transmitters architectures, efficiency, linearity, and/or BW are often still constrained or tradedoff from one another. This is often caused by the nonoptimum drive conditions of the individual branch amplifier due to the passive input signal splitting, inaccurate harmonic control for the active devices (vs. frequency) and losses and BW constrains in the output combiner. In view of this, with the upcoming availability of low-cost high-performance and highly integrated smart drivers [5], active input signal splitting/dual input transmitter signal generation are coming into reach. Consequently, DPAs that make use of branch amplifiers with individually accessible inputs, benefit of better branch amplifier control, facilitating less efficiency degradation at power backoff and support extended wideband operation [6]–[8].

In [9], harmonically matched GaN devices for quasi-load insensitive (QLI) class-E operation, implemented within a standard RF package, were proposed for use in DPA and outphasing configurations. This choice for QLI class-E is based on the very high efficiency that this specific class-E operation can provide over a large load range. A property that is essential to PA concepts that rely on load modulation to enhance their efficiency. Less explored is the frequency range that this particular operation class can provide [10]. Typically, achieving wideband operation is complicated by providing the proper fundamental and harmonic terminations versus frequency. Although various works have been reported, addressing the theory for continuous classes [11], [12], practical DPA implementations still face difficulties in actually providing these optimum conditions at all frequencies within the targeted BW. This paper addresses this problem by integrating the harmonic terminations for QLI class-E operation directly within the transistor package. As such conflicting matching requirements for the (fundamental) and harmonic terminations in practical (wideband) designs can be avoided or strongly mitigated. This enables easy to assemble wideband Doherty and/or highly performance outphasing designs with “class-E like” peak efficiencies, as such enhancing the state of the art.

Manuscript received February 20, 2018; revised June 6, 2018; accepted August 7, 2018. This work was financially supported by the NED University of Engineering and Technology, Karachi, Pakistan, and Ampleon Netherlands B.V. *(Corresponding author: Abdul Raheem Qureshi.)*

A. R. Qureshi is with the Department of Microelectronics, Delft University of Technology, 2628 CD Delft, The Netherlands, and also with the Department of Electronics Engineering, NED University of Engineering and Technology, Karachi 75270, Pakistan (e-mail: a.r.qureshi@tudelft.nl; raheem.qureshi@ampleon.com; araheemqureshi@neduet.edu.pk).

M. Acar is with NXP Semiconductors, 6534 AE Nijmegen, The Netherlands (e-mail: mustafa.acar@nxp.com).

S. C. Pires is with Ampleon Netherlands B.V., 6534 AV Nijmegen, The Netherlands (e-mail: sergio.pires@ampleon.com).

L. C. N. de Vreede is with the Department of Microelectronics, Delft University of Technology, 2628 CD Delft, The Netherlands (e-mail: l.c.n.devreede@tudelft.nl).

Color versions of one or more of the figures in this paper are available online at http://ieeexplore.ieee.org.

Digital Object Identifier 10.1109/TMTT.2018.2868876

This paper continues and further develops the work of [9] in the following aspects. The theoretical background of QLI class-E devices, featuring optimum package integrated harmonic terminations and their operation is presented. Using these devices, a new wideband QLI class-E matched Doherty has been analyzed, optimized, experimentally verified, and benchmarked against the current state-of-the-art base-station transmitter design.

This paper is organized as follows. In Section II, QLI class-E is discussed, and the actual package integration is given and evaluated. In Section III, the simulated and measured load–pull results of package integrated low-pass QLI class-E are provided. Sections IV and V describe the theory of QLI class-E matched wideband DPA operation and conclude with the newly designed and realized compact wideband DPA with its measurement results. Finally, conclusions are drawn in Section VI.

II. Package Integrated Low-Pass QLI Class-E

QLI class-E operation (Fig. 1) can offer high efficiency for load modulating amplifiers within a small form factor [10], [13]–[15]. It is a "finite inductor" class-E configuration, in which the inductance of the drain bias choke is intentionally reduced. In [16], it was shown that for the class-E topology of Fig. 1(a), the selection of the resonance factor ($q = 1/\omega\sqrt{LC}$), strongly affects the class-E switching operation. For instance, in the case of conventional class-E ($q = 0$, with L approaching infinity), when the value of R_L increases, the voltage at the turn-ON time is no longer zero and starts to increase, yielding increased capacitive power losses [Fig. 1(b)]. In comparison, for QLI mode ($q = 1.3$), the output voltage at the actual switching moment always stays close to zero for a large range of R_L, thus avoiding any capacitive switching losses [Fig. 1(c)]. In fact, $q = 1.3$ represents a distinct optimum, which provides optimum drain efficiency over a very large range of load resistance(s), which is a unique property compared to the other popular choices like the parallel resonant class-E [16] [Fig. 1(d)]. Note that the efficiency can also be plotted versus R_L for different values of (q) as originally was shown in [4].

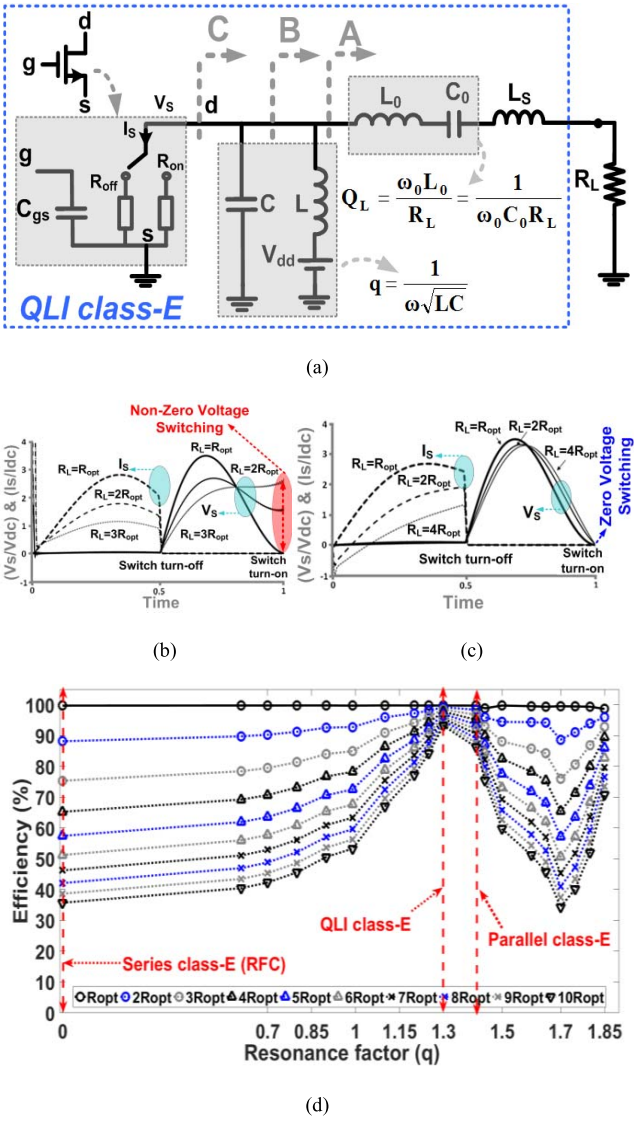

(a) (b) (c) (d)

Fig. 1. QLI class-E. (a) Principle schematic of the finite dc feeds inductor configuration with series resonator. (b) Waveforms when the resonance factor $q = 0$ and (c) when $q = 1.3$. (d) Efficiency as a function of resonance factor q at frequency = 2.14 GHz for loading conditions that represent a multiple of the optimum load value for reaching MXE.

A. Implementation Package Integrated Low-Pass QLI Class-E Devices

For the circuit of Fig. 1(a), the circuit element values can be found using the equations from [9] and [16] for $q = 1.3$. However, when considering practical RF power devices, mounted within "standard" RF packages [12], [17]–[20], size, cost, and bias feed constraints limit the number of practical matching network topologies. In view of this, the use of a series resonator proves to be troublesome, since it requires the addition of a separate bias path connection to the RF package, with associated decoupling. Therefore, replacing the series resonator by a low-pass LC section (L_1C_1) [Fig. 2(a)] is an attractive alternative [19]. However, since this topology deviates from the traditional class-E topology, its elements values need to be reidentified. A procedure to do this is given in the Appendix, which provides the element values for the low-pass QLI class-E circuit of Fig. 2(a) that closely approximates the fundamental and harmonic load conditions presented to the internal active device of the classical QLI class-E case. When going from Fig. 2(a) to a package integrated implementation, the capacitance C_1 can be realized by using the lead frame capacitance in parallel with an additional discrete capacitor C_P, which can be connected by multiple bond wires in parallel, here, represented by their effective inductances L_a and L_b [Fig. 2(b)]. Since these bondwires can be kept very small, in most practical cases, their inductances can be neglected.

In this paper, we target QLI class-E design featuring a 9.6-mm 0.25-μm GaN HEMT mounted in an SOT1135 package intended for operation at 2.14 GHz. To obtain the required circuit parameters, we first use [16] to obtain the elements for the classical QLI class-E configuration of Fig. 1(a)

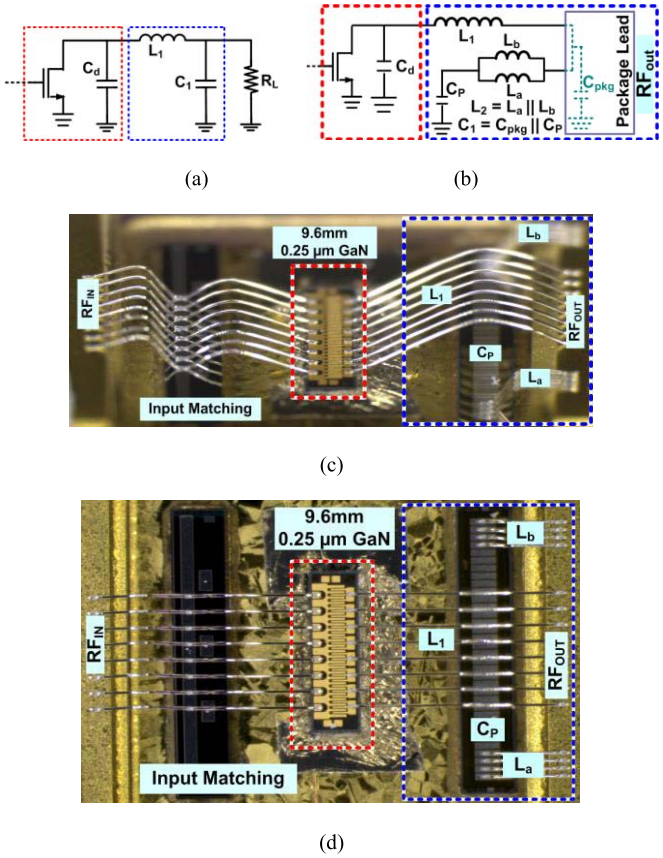

Fig. 2. QLI class-E low-pass circuit configuration. (a) Simplified schematic. (b) Schematic for package implementation (L_a and L_b are very small). (c) Side view and (d) top view of physical network implemented inside standard Ampleon SOT1135A package.

and the Appendix for determining the circuit values for the QLI low-pass class-E configurations of Fig. 2(a) and (b). Their circuit parameters are given in the Appendix. The related package integrated QLI class-E device is shown in Fig. 2(c) and (d). Using this configuration, the fundamental QLI class-E impedance is effectively provided by C_d in combination with the low-pass L_1C_1 network and external offered fundamental impedance, while the long bond wires used for the implementation of L_1 provide high impedance for the harmonic frequencies, as such effectively isolating the active device from any external harmonic loading outside the package. Practical guidelines for designing package integrated PAs can be found in [21].

The Smith chart presented in Fig. 3 gives the fundamental and harmonic loading conditions offered to the active device for the various schematics and implementations. Namely, for the classical class-E topology of Fig. 1(a) with $q = 1.3$, as analytically predicted by (9) in the Appendix. In addition, the related simulation results of the circuit of Fig. 1(a). The simulation results of the low-pass QLI class-E circuit of Fig. 2(a) and its more practical version for package integration Fig. 2(b). In conclusion, also the fundamental and harmonic loading conditions offered to the active device as predicted by the HFFS modeled SOT1135A package with its lead frame, all bond wires and C_d, as shown in Fig. 2(c) and (d), have been

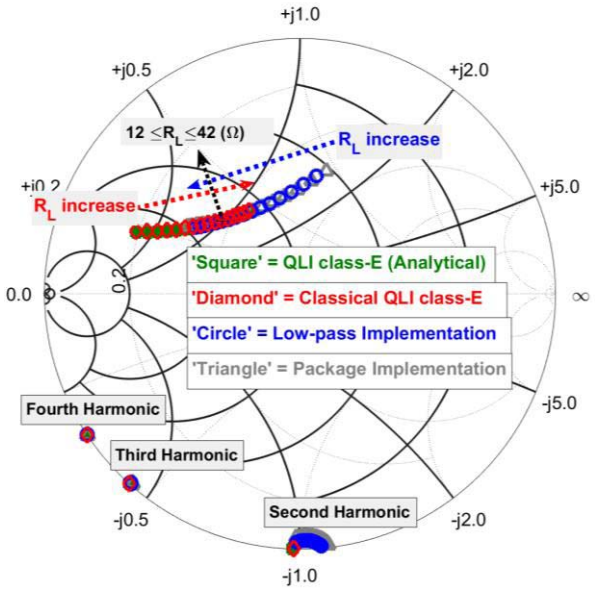

Fig. 3. Admittances plot (fundamental, second, third, and fourth harmonics) as a function of R_L swept from $12 \leq R_L \leq 42$ (Ω) for the QLI class-E: analytical solution using (9), simulation response of the circuits given in Fig. 1(a) and the low-pass implementation is given in Fig. 2(a) and package implementation estimation is given in Fig. 2(b).

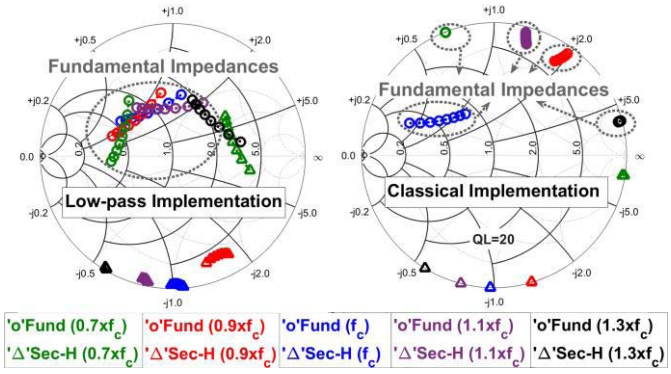

Fig. 4. Comparison of the frequency dependence of the classical and low-pass QLI class-E implementations for a changing R_{opt} load at various (normalized) frequencies.

added to the Smith chart of Fig. 3. All QLI configurations show an excellent agreement with the theoretical optimum terminations for QLI class-E operation as provided by (9) in the Appendix. It can be seen from Fig. 3, however, that when varying the fundamental load R_L, its impedance change is basically "inverted" for the drain node of the active device due to the low-pass QLI load network that approximates a "lumped" impedance inverter. We will make use of this impedance inversion in our Doherty transmitter in Section IV.

B. Bandwidth Considerations Class-E Output Topologies

The frequency response of the classical and low-pass QLI class-E output networks are compared in Fig. 4. Here, as a function of the normalized frequency (from $0.7 \times f_c$ to $1.3 \times f_c$), the load (R_{opt}) has been swept and the resulting admittances for fundamental and harmonics have been plotted.

Due to the (narrowband) series resonator (QL = 20), the fundamental admittance for the classical class-E configuration proves to be very sensitive to the operating frequency (f_c). As we can see in Fig. 4, $a\pm15\%$ change in operation frequency has a huge impact, causing the fundamental impedance to jump almost to the edge of the Smith chart. The low-pass QLI class-E fundamental configuration appears to be more immune, although its Γ_{drain} rotates versus frequency due to the delay of the low-pass network, this behavior is easy to absorb in a wideband DPA design, as we will discuss in Section IV.

III. Characterization of the Package Integrated Low-Pass QLI Class-E Devices

The simulated and measured efficiency and output power contours (load–pull data) of the (9.6-mm 0.25-μm GaN) package integrated low-pass QLI class-E ($q = 1.3$) device at 2.14 GHz, as a function of the provided external fundamental load (Z_{ref} Smith chart = 10 Ω) are shown in Fig. 5(a) and (b), respectively. Since the harmonics are terminated inside the RF package, conventional fundamental load–pull is sufficient to obtain the maximum efficiency (MXE), maximum output power (MXP), and the optimum trajectory for efficiency versus power backoff. Measured and simulated load–pull data show that both MXE and MXP are indeed aligned on the real axis of the Smith chart, allowing the preservation of the peak efficiency while output power is varied by the real part of the load (R_L). This property is very useful in boosting the average efficiencies of Doherty and outphasing PAs.

Furthermore, to validate the wideband property of low-pass QLI class-E, the measured and simulated linear programming (LP) data are also compared from 1.8 to 2.4 GHz and their results are summarized in Fig. 5(c) and (d). On each frequency, the simulated and measured output power (dBm) and efficiency are compared by changing the fundamental load from Z_1 (peak power) to Z_4 (BO power level). As one can observe the correlation between simulated and measured results is good, and it shows that the load insensitive property of low-pass class-E is very well maintained over a wide range of frequencies.

IV. Dual Input DPA Using Package Integrated Low-Pass QLI Class-E Devices

The previously described packaged integrated low-pass QLI class-E device has power and efficiency contours that are perfectly aligned on the real axis of the Smith chart [Fig. 5(b)], providing evidence for the ∼90° phase rotation inside the package. This internal lumped $\lambda/4$ line is beneficial in the design of load modulating amplifiers, since it can act directly as the impedance inverter for the main device in a DPA [Fig. 6(a)]. In addition, it also eliminates the need for offset line or prematch for the peaking device as commonly applied in (conventional) DPA design [Fig. 6(c)] [22]. Note that, in this approach, the connecting $\lambda/4$ transmission line (QWTL) in combination with the internal lumped $\lambda/4$ line in the peak branch devices [Fig. 6(d)] provides the $\lambda/2$ connection/parallel resonator [Fig. 6(b)] that proves to be very favorable in achieving a high-efficiency BW at the power BO point.

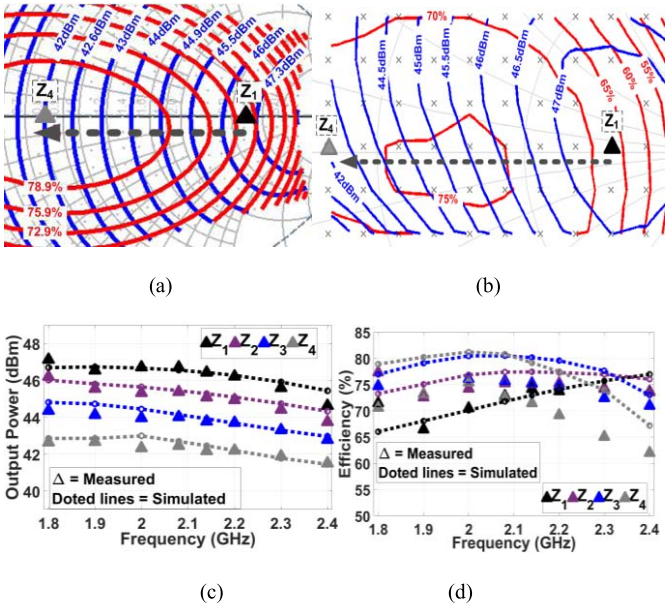

Fig. 5. 9.6-mm 0.25-μm GaN QLI class-E device results. (a) Simulated LP data at 2.14 GHz with $Z_{\text{ref}} = 10$ Ω. (b) Measured LP at 2.14 GHz with $Z_{\text{ref}} = 10$ Ω. (c) Comparison between simulated and measured output power versus frequency at different impedance levels. (d) Comparison between simulated and measured efficiency versus frequency at different impedance levels.

The $\lambda/2$ line can compensate for the otherwise strongly varying frequency-dependent impedance behavior offered to the main device [Z_2 in Fig. 6(b)] [23], [24] or [Z_4 in Fig. 6(d)].

The simulated response of the (idealized) circuit of Fig. 6(d) under single-tone excitation is shown in Fig. 7. The QLI class-E impedance matched main and peaking devices are biased close to their threshold voltage. Their driving gate–source voltage profiles are chosen such that the resulting (fundamental) currents of the main and peak device mimic the well-known profile of a symmetric DPA [25]. The FET transistors in these idealized simulations are modeled as voltage-controlled resistors (linear region FET) if their time-varying gate–source voltage is higher than their threshold voltage ($V_{\text{gs}} > V_T$) and is open ($R_{\text{OFF}} = \infty$) when ($V_{\text{gs}} < V_T$). Furthermore, all drain capacitances are modeled by the equivalent parallel capacitance C_d as shown in Fig. 6(d).

In deep BO, the peaking device will be OFF ($I_P = 0$). The main device will start to modulate its output resistance/conductance through $V_{\text{gs}}(t)$ when $V_{\text{gs}}(t) > V_T$, with the result that I_m starts to increase with increasing $V_{\text{gs}}(t)$ [see Fig. 7(a)] and V_m starts to be modulated. Note that these excursions are first insufficient to go directly into voltage saturated class-E operation. In fact, due to these small excursions and the used QLI class-E terminations, a "soft class-E" or "class-J" like operation is initiated, which can be seen by inspecting the voltage waveform at these lower power levels [Fig. 7(a)]. However, as we increase the input drive, the main device enters eventually into voltage saturation and pure QLI class-E operation is reached. At 6-dB BO, the peaking device starts to conduct [Fig. 7(c)] in a similar way as previously described for the main device.

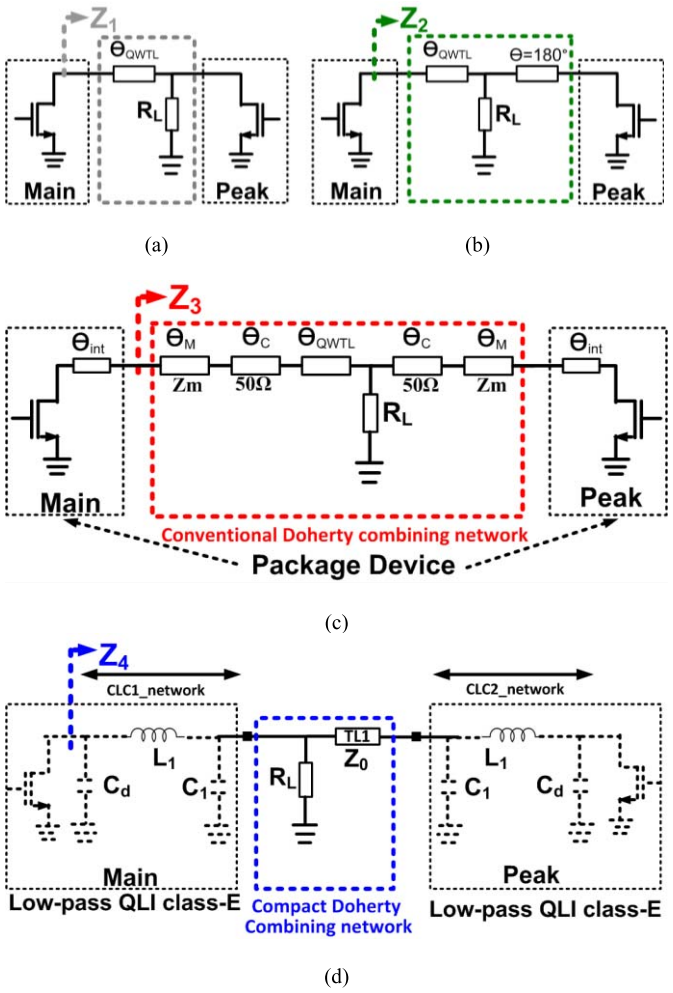

Fig. 6. (a) Classical class-B Doherty. (b) Modified wideband class-B Doherty. (c) Conventional class-B Doherty configuration using package device with Θint internal rotation. (d) Proposed compact Doherty configuration featuring QLI class-E operation.

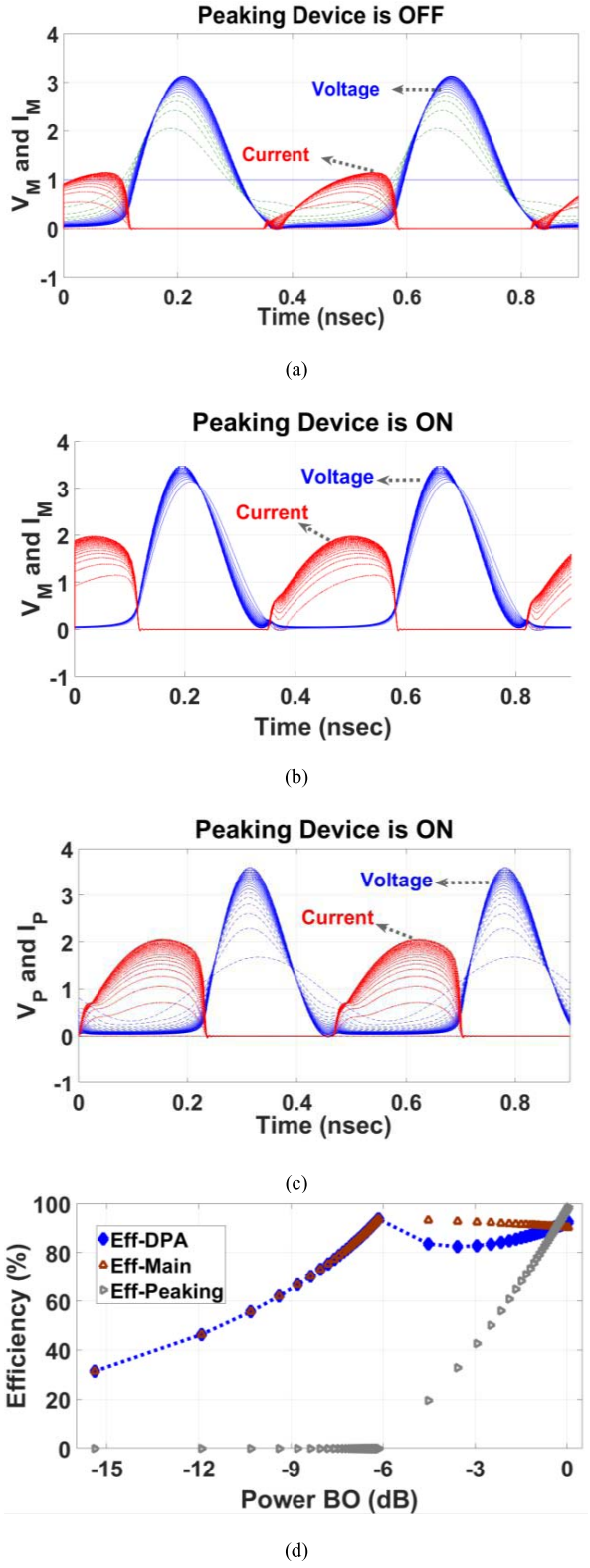

Fig. 7. Simulated intrinsic voltage and current waveform at drain terminal of Main and Peak devices (QLI class-E) in Doherty configuration. (a) V_M and I_M at BO power levels (peak is OFF). (b) V_M and I_M at maximum power levels (peak is ON). (c) V_P and I_P at maximum power level. (d) Efficiency as a function of BO power level.

However, from 6-dB power backoff to full power, the main device remains in pure QLI class-E and thus at its MXE, while its current I_m still increases due to the DPA load modulation [note the similarity with Fig. 1(c)]. Also, at the full power, the peaking device has reached pure QLI class-E operation with associated high efficiency [Fig. 7(d)]. As one can observe, the efficiency potential of the proposed QLI class-E DPA is indeed significantly higher than that of a classical class-B Doherty.

The simulation results of the proposed idealized wideband low-pass QLI class-E DPA, a conventional ideal class-B Doherty, and a wideband class-B Doherty [23] are shown in Fig. 8. As expected, the classical Doherty topology [26] shows a strong efficiency dependence versus frequency at 6-dB power backoff, while at the full power, the efficiency basically remains constant versus frequency at ∼78.5% (assuming perfectly shorted harmonics at all times). When applying the $\lambda/2$ resonator in the path of the peaking amplifier, the impedance offered to the main device becomes much better behaved versus frequency, as it is reflected in the related efficiency BW [Fig. 8(b)]. When considering the efficiency at the center frequency, the proposed low-pass QLI class-E DPA [Z_4 in Fig. 6(d)] benefits from class-E like efficiency approximating 100% peak efficiency at the center frequency.

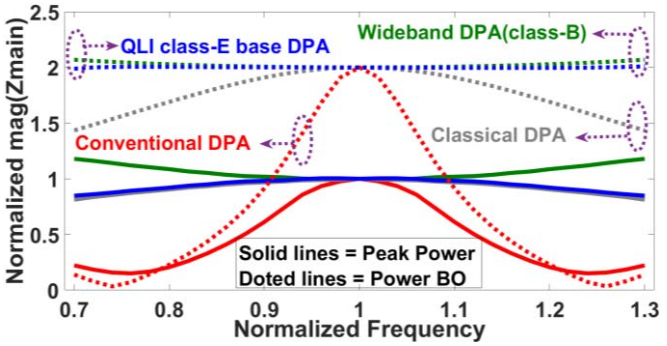

(a)

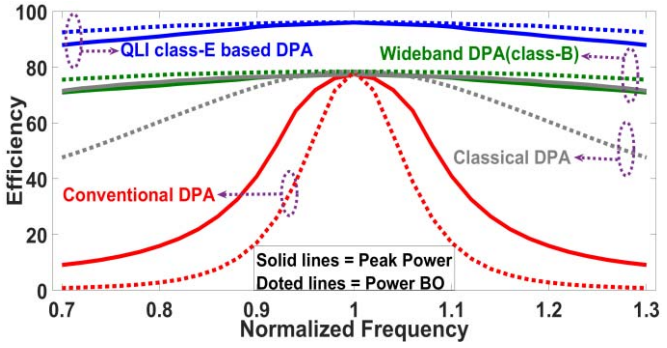

(b)

Fig. 8. Simulated response for the Doherty configurations of Fig. 7, namely, the classical Doherty [Fig. 7(a), in gray], improved wideband class-B Doherty [Fig. 7(b), in green], conventional Doherty [Fig. 7(c), in red], and the low-pass QLI class-E compact Doherty combiner [Fig. 7(d), in blue] as function of frequency at 0-dB (solid lines) and 6-dB power backoff (dashed lines). (a) Z_{main}. (b) Efficiency.

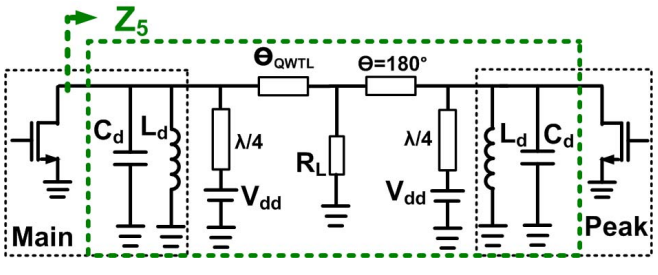

(a)

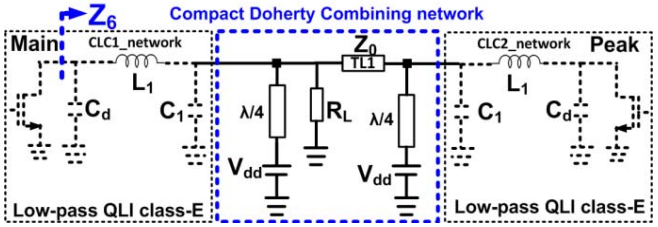

(b)

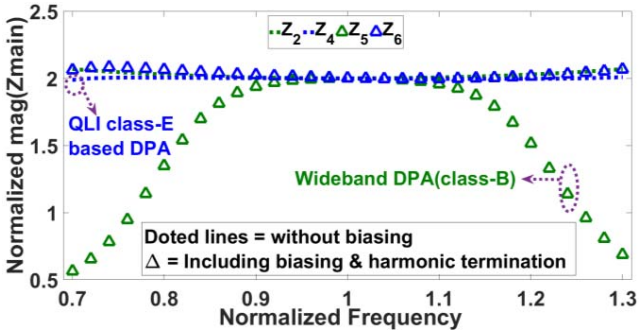

(c)

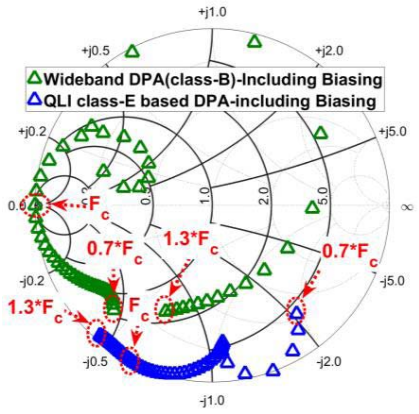

(d)

Fig. 9. (a) Principle schematic of a wideband class-B Doherty with inshin to resonate out C_d and $\lambda/4$ biasing stubs to provide the second harmonic terminations. (b) Principle schematic of wideband QLI class-E Doherty including $\lambda/4$ biasing lines. (c) Simulated response for the wideband class-B Doherty using ideal (frequency independent) harmonic shorts and with the realistic stubs for biasing and second harmonic terminations of Fig. 9(a) and (b). (d) Comparison of frequency dependence of second harmonic termination offered to the drain of the active device for the improved wideband class-B Doherty (Z_5) and low-pass QLI class-E Doherty (Z_6).

Also, here, the use of the $\lambda/2$ resonator in the peak amplifier path improves the behavior of the impedance offered to the main device, allowing very high-efficiency wideband behavior both at peak power and in power backoff operation. When including stubs for providing the bias to the active devices as shown in Fig. 9(a) and (b), we see that the fundamental and harmonic impedances offered to the main device versus BW are only weakly affected in case of low-pass QLI class-E operation [Fig. 9(c) and (d)]. In contrast, when aiming for wideband class-B DPA operation [Fig. 9(a)], the fundamental and harmonic impedances offered to the main device in power backoff versus frequency show larger variations, which prevent wideband operation with a single-ended design approach. Note that push–pull wideband class-B DPA designs [27] can overcome these limitations but only at the cost of a more complicated assembly and balun which tends to add more losses.

V. Measurement Results of Wideband DPA

To experimentally verify the low-pass QLI class-E DPA featuring the dedicated packaged devices, a very compact DPA has been realized (Fig. 10). The Doherty prototype is designed on 30-mil-thick Roger substrate with copper microstrip lines of 35 μm thickness using the electromagnetic simulator of ADS. To ensure DPA operation, a soft rolloff from the switch-mode class-E operation is required. This has been achieved by biasing the main device close to its threshold voltage in "class-AB" like conditions to achieve sufficient gain, while the peak device is biased more toward "class-C" to reduce the

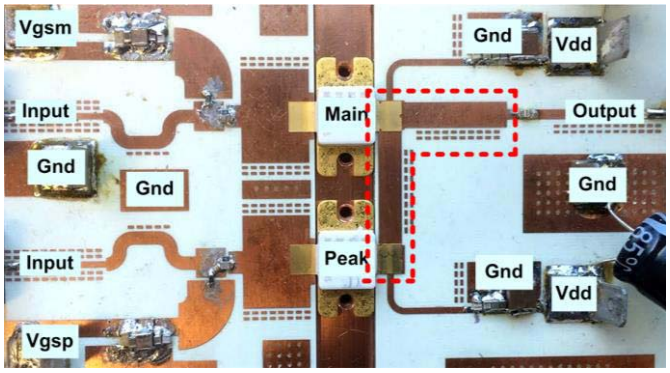

Fig. 10. Hardware prototype of the proposed compact wideband DPA featuring QLI class-E operation.

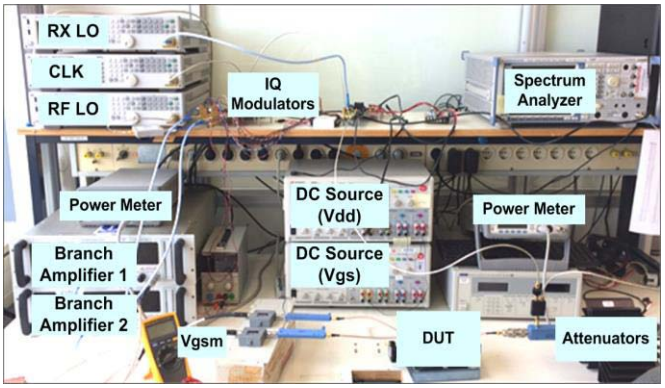

(a)

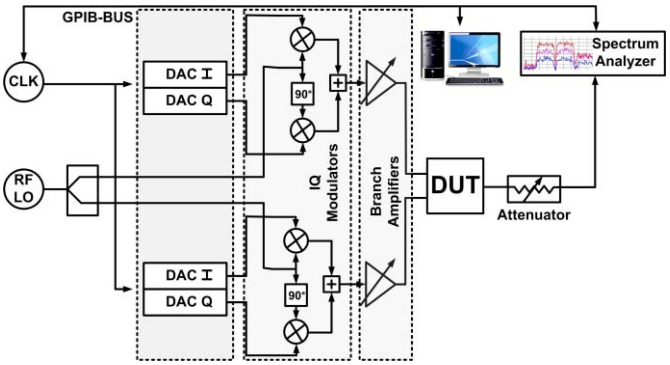

(b)

Fig. 11. (a) Dual input measurement setup. (b) Block diagram representation.

impact of its quiescent current. The drain supply voltage V_{dd} is set to 28 V. As discussed, due to the harmonic terminations provided, both devices start in class-J like operation and when hard driven enter QLI class-E operation. The amplifier is tested using the dual-input characterization setup of Fig. 11(a), which architecture is given by the block diagram of Fig. 11(b).

For linearization, the algorithm of vector switch generalized memory polynomial (VS-GMP) for digital predistortion (DPD) presented in [28] is used. Following the notation of [28], the parameters used were: $P = 5$, $M = 2$, $G = 1$, and $N = 15$, in which P is the order of the nonlinearity, M is the memory depth, G is the number of cross terms according

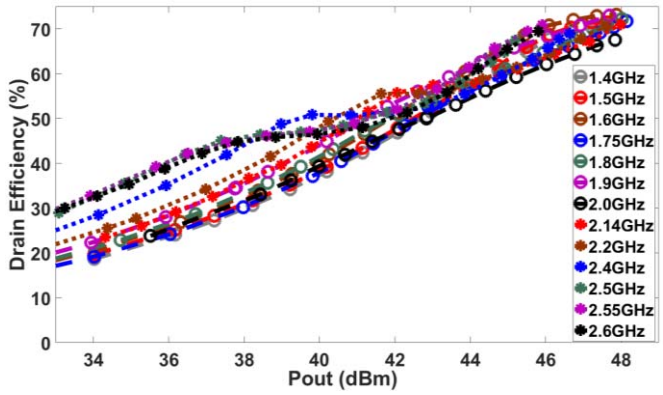

(a)

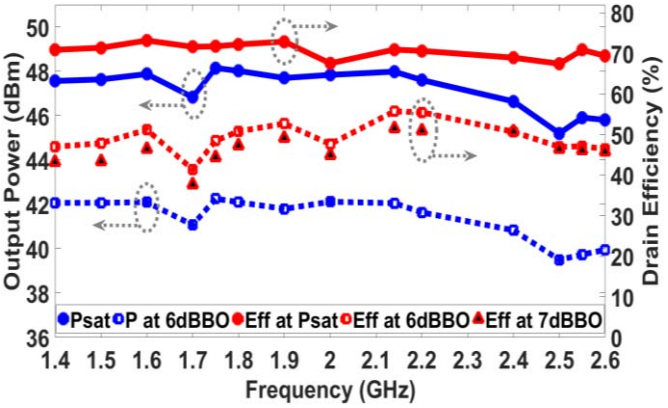

(b)

Fig. 12. Static measurement of wideband DPA. (a) Drain efficiency as a function of output power on different frequencies. (b) Output power and drain efficiency (at saturation and BO levels) as a function of frequency.

to the GMP definition, and N is the number of regions in the VS-GMP model.

Using this setup, the DPA has been measured over the 1.4–2.6 GHz frequency range. Although the test setup is capable of sweeping the relative phase difference, as well as the power of the input signals, in these DPA measurements, the relative phase difference of the two inputs is kept constant and only input power has been swept. Since the workbench used does not support pulsed operation, the DPA devices were not pushed into high compression to avoid thermal damage. The measured efficiency of the proposed low-pass QLI class-E DPA as a function of the output power and frequency is shown in Fig. 12(a). As one can observe, the typical two-way symmetric Doherty high-efficiency region is present. Fig. 12(b) shows the variation in output power and efficiency as a function of the frequency. One can note that the proposed DPA can deliver 48-dBm saturated output power (P_{sat}) at 2-dB gain compression. There is a small drop in output power beyond 2.4 GHz as shown in Fig. 12(b). The efficiency at P_{sat}, 6-dB BO, and 7-dB BO of the amplifier as a function of frequency is shown in Fig. 12(b). At $P_{sat} = 48$ dBm, the amplifier maintains almost 71% efficiency ($\pm 3\%$) over the entire band of 1200 MHz (1.4–2.6 GHz). When testing with a single-carrier Long-Term Evolution (LTE) with

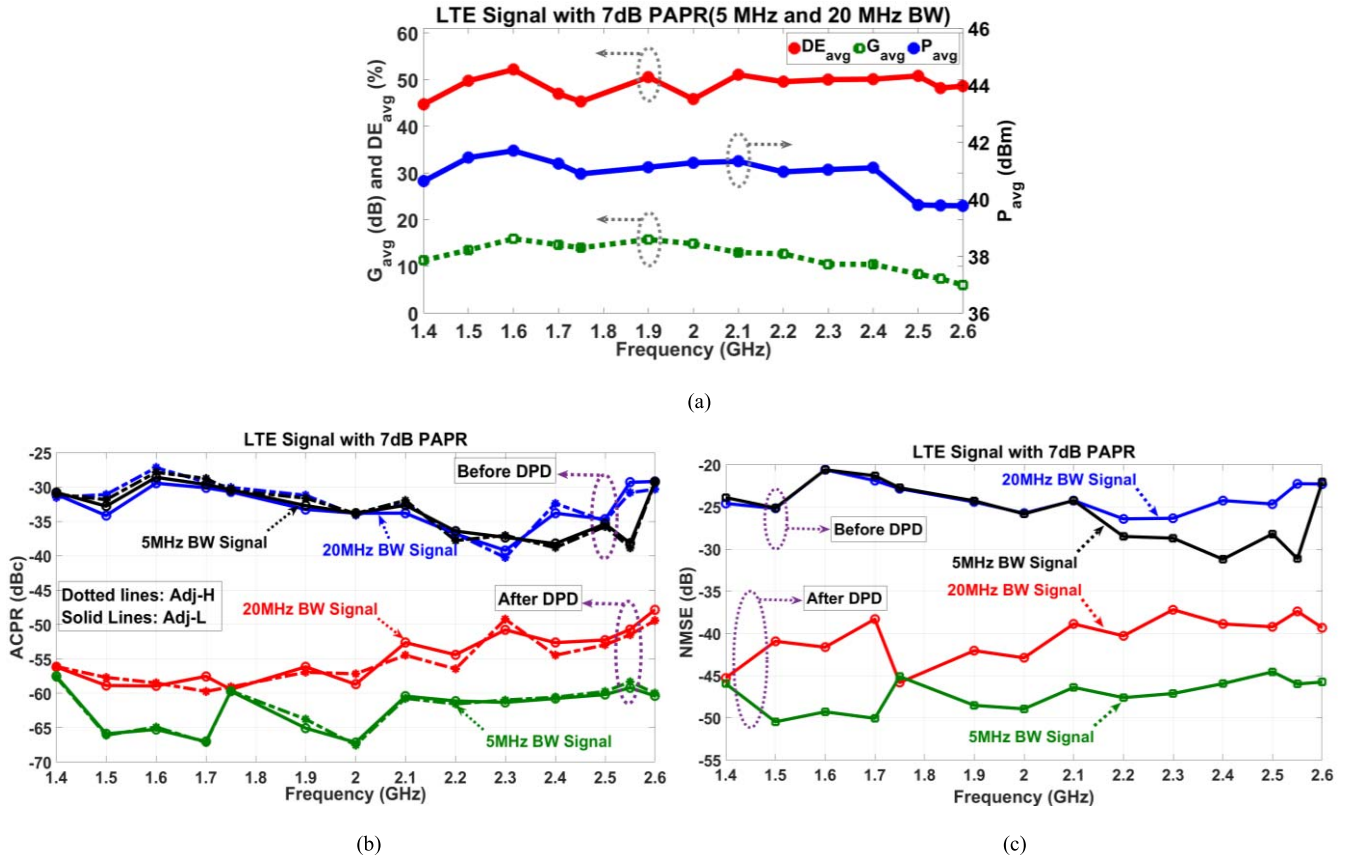

Fig. 13. Dynamic measurement of dual input DPA with LTE 5- and 20-MHz modulated signals with 7-dB PAPR. (a) Average output power (P_{avg}), drain efficiency (DE_{avg}), and gain (G_{avg}) versus frequency. (b) ACPR before and after DPD versus frequency. (c) NMSE before and after DPD versus frequency.

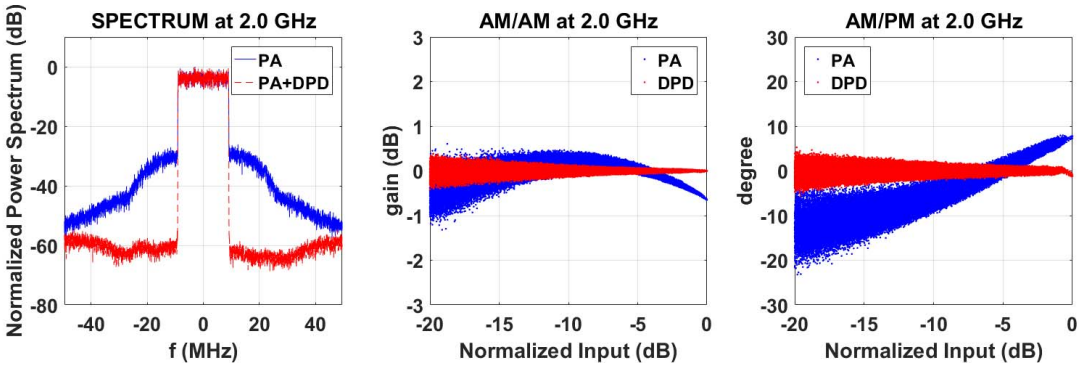

Fig. 14. Measured spectra, AM/AM, and AM/PM of dual input DPA at 2.0-GHz center frequency with modulated signal LTE 20-MHz 7-dB PAPR ($P_{\text{avg}} = 41$ dBm).

7-dB PAPR using 5- and 20-MHz BW signals, the average efficiency is 49% (±3%) over the 1.4–2.6 GHz band [Fig. 13(a)], which represents a 60% fractional BW. The related gain (G_{avg}) is ∼13 dB and the associated output power (P_{avg}) is 40 dBm (±1 dB). Compared to other works, as shown in Table I, the variation in average power and efficiency is very small for this 60% fractional BW, which is one of the strongest aspect of the proposed low-pass QLI class-E DPA operation mode. Namely, in [27] and [29]–[31], the variation in average efficiency are ±9%, ±7%, ±9%, and ±8.5%, respectively. The gain at the high frequencies of the band could be improved by further optimizing the input matching network of the GaN devices at these frequencies. Since due to higher reflection losses, the gain is lower.

On average, the proposed DPA maintains the adjacent channel power ratio (ACPR) level below −60 and −53 dBc after DPD for 5- and 20-MHz LTE signals as shown in Fig. 13(b). It was observed that the low and high side ACPRs are similar to each other in case of a 5- and 20-MHz BW LTE signal. The normalized mean square error (NMSE) behavior before and after DPD as a function of frequency is shown in Fig. 13(c). For the entire frequency range, the NMSE

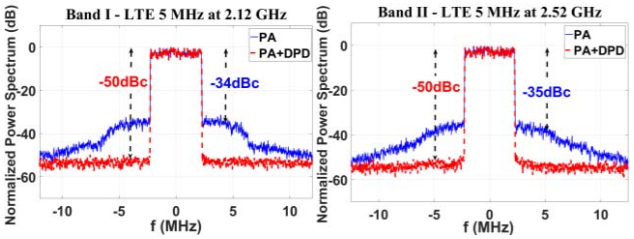

Fig. 15. Measured amplifier output spectra before and after linearization when driven with 5-MHz LTE signal at 2.12 and 2.52 GHz (IBW = 400 MHz).

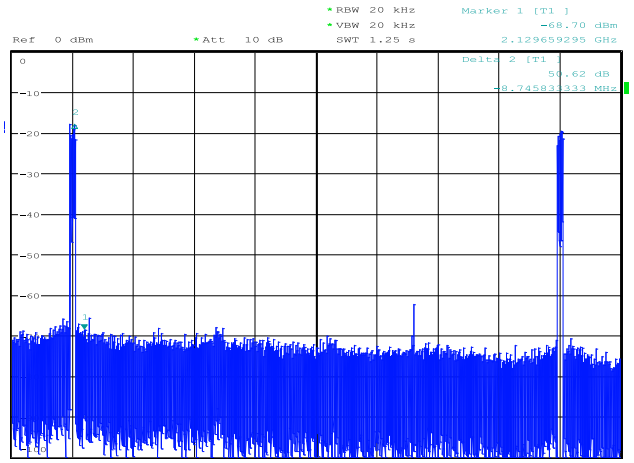

Fig. 16. Measured amplifier full output spectra directly captured from spectrum analyzer (SPA) when driven with 5-MHz LTE signal at 2.12- and 2.52-GHz (IBW = 400 MHz) SPA SPAN = 500 MHz.

values of the proposed DPA are below −45 and −36 dB for 5- and 20-MHz LTE signal, respectively. The measured output spectrum, amplitude-to-amplitude (AM/AM), and amplitude-to-phase (AM/PM) distortion before and after the application of the DPD for the 20 MHz, 7-dB PAPR LTE signal case with center frequency of 2 GHz at $P_{\text{avg}} = 41$ dBm are shown in Fig. 14 as a reference. The excellent linearizability of the proposed wideband Doherty was further validated by testing with a dual-band scenario, which is of high interest to base station manufacturers that want to use a (single) TX line-up in support of multiple simultaneous data links in different wireless bands. For this dual-band scenario, the DPD algorithm of [32] was used. This model not only compensates for the intermodulation distortion in each band but also for the cross-modulation distortion, allowing to obtain high signal accuracy in both bands. The spectrums before and after DPD are shown in Fig. 15. Before DPD, the ACPR for both bands was noted as −34 and −35 dBc, which after DPD improves to −50 and −50 dBc, with at an average output power of 40 dBm and an average efficiency of 42%, which is slightly less due to the increased PAPR of 8 dB of the combined signals. As an additional support for the excellent spectral purity achieved in this dual-band operation, the full spectrum is given in Fig. 16. Consequently, the proposed PA exhibits excellent linear amplification with low memory effects for carrier aggregation using two LTE signals with 400-MHz separation.

VI. Conclusion

In this paper, low-pass QLI class-E matched devices for use in Doherty and mixed-mode outphasing transmitters have been evaluated. These QLI class-E matched devices provide very high efficiency even for strongly varying loads, a property that is essential to load modulating transmitters. The proposed low-pass output matching is compatible with package integration and can be dimensioned such that it acts like a lumped $\lambda/4$ impedance inverter for the fundamental frequency, while all higher harmonics are effectively terminated inside the RF package and isolated from the external circuitry. These two properties allow designers to develop very simple, compact, and very wideband output power combining networks that enable class-E like peak efficiency numbers. To support the above mentioned, a comparison is given for the achievable efficiency versus BW in classical, as well as recently proposed wideband DPA configurations. The introduced package integrated matching technique, combined with a wideband DPA topology can provide high efficiency over a large BW, with very low fluctuation in efficiency and output power. The realized Doherty and mixed-mode outphasing transmitter demonstrators of [9] were measured on a dual input test bench, which is capable of sweeping both amplitude and relative phase of the generated input signals as well as provide modulated signals. The realized wideband low-pass class-E DPA demonstrates 49(±3)% average efficiency over 60% relative BW (1.4–2.6 GHz) for 7-dB PAR LTE signals, while showing excellent linearizability in both single carrier, as well as multiband LTE/WCDMA scenarios (ACPR better than −50 dBc). When the proposed devices are applied in mixed-mode outphasing transmitter 67% average efficiency can be obtained with a comparable linearity performance [9].

Appendix

In this appendix, we give the procedure to determine the optimum circuit element values for the low-pass QLI class-E configurations of Fig. 2. To do so, first, we determine the optimum loading conditions of the classical QLI class-E network topology of Fig. 1(a), while making use of the class-E parameter definitions of [9] and [16], namely,

$$K_L = \omega_o L / R_L \tag{1}$$

$$K_C = \omega_o C R_L \tag{2}$$

$$K_X = X_S / R_L. \tag{3}$$

For Fig. 1(a), $X_s = \omega_o L_s$, moreover, the impedance is seen at node "A," for the fundamental and harmonic frequencies ($Z_{n,A}$) assuming that series resonator (L_o, C_o) resonates at the design frequency (f_0), can be written as

$$Z_{n,A} = R_L \left[1 + jn\omega_o \left(\frac{L_S}{R_L} + \frac{L_0}{R_L} \left(\frac{n^2 - 1}{n^2} \right) \right) \right]. \tag{4}$$

In which, $n = \omega\sqrt{L_0 C_0}$ (equal to "1" at f_0), represents the harmonic index. We redefine $Z_{n,A}$ as

$$Z_{n,A} = R_L(1 + jA). \tag{5}$$

TABLE I
PERFORMANCE COMPARISON OF QLI CLASS-E-BASED DESIGNS WITH STATE-OF-THE-ART WIDEBAND 2-WAY DPAS

Ref.	[33]	[34]	[30]	[29]	[35]	[27]	[36]	[31]	[37]	[38]	[39]	[40]	[41]	T.W (QLI class-E)		
Remarks	C-Mode	Two-Stage DPA	C-Mode	-	SPA-D [b]	Push-Pull	CCL [c]	Dis. M/C [d]	Sym	-	-	Cont. mod	-	Narrowband DPA [9][e]	Mixed M. Out-phasing [9][f]	Wide band DPA [g]
Year	2017	2017	2016	2016	2016	2015	2015	2014	2012	2013	2018	2016	2015	2017	2017	2018
F_{center} (GHz)	2.2	2	2.2	3.45	0.65	0.64	2	1.8	0.85	2.05	2.65	2.2	2.15	2.14	2.14	2.0
Freq. Range (GHz)	1.7-2.7	1.8 - 2.2	1.65 - 2.75	3.3 - 3.6	0.46 - 0.83	0.522 - 0.762	1.8 - 2.2	1.0-2.6	0.7-1.0	1.7-2.4	1.5-3.8	1.65 - 2.75	1.7-2.6	-	-	1.4 – 2.6
FBW (%)	45.5	20	50	8.69	57	37	20	83.9	35.3	36	87	50	41.9	-	-	60
P_{sat} [a] (dBm)	53.3	46	46	49	51	58.4	42	40	49.9	40.2	42	46	46	-	-	47.2
Max	54.3	45.9	46	49.5	52	59	42.3	40	50.5	41	43.4	46	46.3	46.2	49	48.2
Min	52.7	46.4	45.8	48.5	49.5	57.5	41.7	40	48.9	39	42.3	45.8	44.6	-	-	45.2
DE_{sat} [a] (%)	58	53	68	64	63	58	72	61	67.3	60	54	68	62.3	-	-	71
Max	66	55	77	70	76	62	74	85	74	72	63	77	66	69	77	73
Min	53	50	60	56	43	52	69	45	60	53	42	60	57	-	-	68
DE_{BO} [a] (%)	45	47	59	54	53	48	63	44	60.6	46	42	59	50.8	-	-	49
Max	50	50	67	60	62	50	68	57	68	59	55	67	57	58	60	56
Min	40	45	50	42	42	40	59	31	50	43	33	50	47			41
DE_{Avg} [a] (%)	42	42	52	48	57	44	56	46	-	-	-	52	51	-	-	49
Max	47	45	63	55	-	49	57	52	55	47	33	63	55	58	67	52
Min	38	41	45	41	-	31	53.5	35	-	-	-	45	46	-	-	45
P_{Avg} (dBm)	46	39.3	38	41	43	50.6	33.5	36	39.1	36	34	38	40	40	42.7	41
ACPR (dBc)	45	58	54	30	47.8	-	34	46.3	-49	-40	-48	54	-31	49	52	55
PAPR (dB)	10	9.9	7.5	8	7.25	7.5	9.3	5.4	8.39	9.6	9	7.5	6.5	7	7	7
Sig. BW (MHz)	10	5	20	40[h]	5	-	5	5	20	20	7	20	5	5	5	20
$Gain_{avg}$ (dB)	-	30	10	14.7	-	20	-	-	15.3	10	-	10.5	10	-	-	12

[a] Arthematic mean = (sum of all numeric values/total number of points)
[b] Sequential power amplifier-Doherty; [c] Complex combining load; [d] Distributed matching/combining; [e] Narrowband DPA at V_{dd} = 25 V; [f] Narrowband mixed-mode outphasing at V_{dd} = 28 V; [g] Wideband DPA at V_{dd} = 28 V, [h] two carriers
T.W = This work (at 5MHz BW LTE signal)

With "A" [using (3)] as

$$A = n\left(K_x + \omega_o\left(\frac{L_0}{R_L}\frac{(n^2-1)}{n^2}\right)\right). \tag{6}$$

Similarly, for the admittance

$$Y_{n,A} = \frac{1}{R_L}\left[\frac{1}{(1+A^2)} - j\frac{A}{(1+A^2)}\right]. \tag{7}$$

Finally, the admittances seen from the nodes B and C [Fig. 1(a)] can be written [using (1) and (2)] as

$$Y_{n,B} = \frac{1}{R_L}\left[\frac{1}{(1+A^2)} - j\left\{\frac{A}{(1+A^2)} + \frac{1}{nK_L}\right\}\right] \tag{8}$$

$$Y_{n,C} = \frac{1}{R_L}\left[\frac{1}{(1+A^2)} - j\left\{\frac{A}{(1+A^2)} + \frac{1}{nK_L} - nK_C\right\}\right] \tag{9}$$

which represents the optimum fundamental and harmonics admittances at the drain of the active device in the QLI class-E ($q = 1.3$) case. All related circuit parameters of Fig. 1(a), for a given output power (P_{out}) and supply voltage (V_{dd}), can be found for the QLI class-E ($q = 1.3$) case, by using for K_P, K_L, K_C, and K_X, respectively; 1.2893, 1, 0.5963, and 0.2607 [16]. Furthermore,

$$R_L = K_P V_{\text{dd}}^2 / P_{\text{out}} \tag{10}$$

$$L_0 = Q_L R_L / \omega_o \tag{11}$$

where Q_L is the quality factor of the series resonance circuit (L_0C_0), as shown in Fig. 1(a), with

$$L = K_L R_L / \omega_o \tag{12}$$

$$C = K_C / \omega_o R_L \tag{13}$$

$$L_S = R_L K_X / \omega_o. \tag{14}$$

For our design, we have used 2.14 GHz as center frequency and have set P_{out} equal to 50 dBm. The low-pass wideband QLI design parameters of Fig. 2 can be found as follows.

1) The required shunt capacitance is provided by the device drain capacitance, which can be kept the same ($C_d = C$).

TABLE II
COMPARISON AND DESIGN SUMMARY FOR THREE CLASS-E IMPLEMENTATIONS AT 2.14 GHz

Component	Units	QLI class-E Fig. 1(a) [a]	QLI class-E Fig. 2(a) [b]	QLI class-E Fig. 2(b) [c]
L	nH	2.38	-	-
L_1	nH	-	2.38	2.25
$C=C_d$	pF	1.39	1.39	1.39
R_L	Ω	32	32	32
L_s	nH	0.62	-	-
L_0 (Q_L=20)	nH	47.59	-	-
C_0 (Q_L=20)	fF	116.2	-	-
C_1	pF	-	4	-
L_a=L_b	nH	-	-	0.4
C_P	pF	-	-	0.42

[a] Classical QLI class-E shown in Fig. 1(a)
[b] Low-pass implementation of QLI class-E shown in Fig. 2(a)
[c] Package implementation of low-pass QLI class-E shown in Fig. 2(b)

2) L_1 is derived from $q = 1/\omega\sqrt{L_1 C_d}$ with $q = 1.3$.
3) C_1 is tuned such that the fundamental and harmonic admittances in Fig. 2(a) are very similar to the values provided by an analytical and simulated solution of classical QLI class-E configuration of Fig. 1(a). For the package implementation of Fig. 2(b) and (c), C_1 is realized by the parallel combination of C_P with the parasitic lead capacitance.
4) L_1, L_a, and L_b are implemented using bondwires. (Note that L_a and L_b are kept very small and, therefore, can be neglected.) The desired inductances were achieved by adjusting the number, length, and height of the bondwires in the HFSS simulation environment. The range of realizable values can be found in [21].
5) In the circuit shown in Fig. 2(b), the equivalent model for the passive bondwires and SOT1135A RF package is obtained through HFSS simulations, which is used for the overall ADS simulation of the packaged GaN device in QLI class-E operation.

The component values for the different embodiments are reported in Table II.

ACKNOWLEDGMENT

The authors would like to thank L. Marco, A. Prata, O. Ceylan, and the Prototype Line Team of Ampleon Netherlands B.V., for their technical support and also R. Bootsman of the Delft University of Technology for providing Fig. 1(d).

REFERENCES

[1] R. Quaglia, V. Camarchia, J. J. M. Rubio, M. Pirola, and G. Ghione, "A 4-W Doherty power amplifier in GaN MMIC technology for 15-GHz applications," *IEEE Microw. Wireless Compon. Lett.*, vol. 27, no. 4, pp. 365–367, Apr. 2017.
[2] J. M. Rubio, J. Fang, V. Camarchia, R. Quaglia, M. Pirola, and G. Ghione, "3–3.6-GHz wideband GaN Doherty power amplifier exploiting output compensation stages," *IEEE Trans. Microw. Theory Techn.*, vol. 60, no. 8, pp. 2543–2548, Aug. 2012.
[3] J. H. Qureshi *et al.*, "A 90-W peak power GaN outphasing amplifier with optimum input signal conditioning," *IEEE Trans. Microw. Theory Techn.*, vol. 57, no. 8, pp. 1925–1935, Aug. 2009.
[4] D. A. Calvillo-Cortes *et al.*, "A package-integrated Chireix outphasing RF switch-mode high-power amplifier," *IEEE Trans. Microw. Theory Techn.*, vol. 61, no. 10, pp. 3721–3732, Oct. 2013.
[5] M. Mehrpoo, M. Hashemi, Y. Shen, R. van Leuken, M. S. Alavi, and L. C. N. de Vreede, "A wideband linear direct digital RF modulator using harmonic rejection and I/Q-interleaving RF DACs," in *Proc. IEEE Radio Freq. Integr. Circuits Symp. (RFIC)*, Jun. 2017, pp. 188–191.
[6] R. Darraji and F. M. Ghannouchi, "Digital Doherty amplifier with enhanced efficiency and extended range," *IEEE Trans. Microw. Theory Techn.*, vol. 59, no. 11, pp. 2898–2909, Nov. 2011.
[7] R. Darraji, F. M. Ghannouchi, and O. Hammi, "A dual-input digitally driven Doherty amplifier architecture for performance enhancement of Doherty transmitters," *IEEE Trans. Microw. Theory Techn.*, vol. 59, no. 5, pp. 1284–1293, May 2011.
[8] A. Ahmed, Y. Wei, J. Staudinger, S. De Meyer, D. Scatamacchia, and B. Branger, "Line-up efficiency improvement using dual path Doherty power amplifier," in *Proc. Eur. Microw. Conf.*, Oct. 2013, pp. 275–278.
[9] A. R. Qureshi, M. Acar, S. Pires, and L. C. N. De Vreede, "High efficiency RF power amplifiers featuring package integrated load insensitive class-E devices," in *IEEE MTT-S Int. Microw. Symp. Dig.*, vol. 1, Jun. 2017, pp. 2029–2032.
[10] F. H. Raab, "Effects of circuit variations on the class E tuned power amplifier," *IEEE J. Solid-State Circuits*, vol. JSSC-13, no. 2, pp. 239–247, Apr. 1978.
[11] D. Y.-T. Wu and S. Boumaiza, "10W GaN inverse class F PA with input/output harmonic termination for high efficiency WiMAX transmitter," in *Proc. IEEE 10th Annu. Wireless Microw. Technol. Conf.*, Apr. 2009, pp. 1–4.
[12] K. K. Sessou and N. M. Neihart, "An integrated 700–1200-MHz class-F PA with tunable harmonic terminations in 0.13-μm CMOS," *IEEE Trans. Microw. Theory Techn.*, vol. 63, no. 4, pp. 1315–1323, Apr. 2015.
[13] N. O. Sokal and A. D. Sokal, "Class E-A new class of high-efficiency tuned single-ended switching power amplifiers," *IEEE J. Solid-State Circuits*, vol. JSSC-10, no. 3, pp. 168–176, Jun. 1975.
[14] F. You, C. Huang, and S. He, "A waveform-verified broadband class-E power amplifier design utilizing finite number of harmonics," in *Proc. IEEE Asia–Pacific Microw. Conf. (APMC)*, Nov. 2017, pp. 988–991.
[15] T. Sharma, P. Aflaki, M. Helaoui, and F. M. Ghannouchi, "Broadband GaN Class-E power amplifier for load modulated delta sigma and 5G transmitter applications," *IEEE Access*, vol. 6, pp. 4709–4719, 2018.
[16] M. Acar, A. J. Annema, and B. Nauta, "Analytical design equations for class-E power amplifiers," *IEEE Trans. Circuits Syst. I, Reg. Papers*, vol. 54, no. 12, pp. 2706–2717, Dec. 2007.
[17] V. Carrubba *et al.*, "Internally-packaged-matched continuous inverse class-FI wideband GaN HPA," in *Proc. 11th Eur. Microw. Integr. Circuits Conf. (EuMIC)*, Oct. 2016, pp. 233–236.
[18] N. Kosaka, E. Kuwata, M. Hangai, K. Yamanaka, T. Yamasaki, and H. Koyama, "A high efficiency GaN HEMT high power amplifier at L-band," in *Proc. Asia–Pacific Microw. Conf.*, Nov. 2014, pp. 789–791.
[19] K. Shi, D. A. Calvillo-Cortes, L. C. N. De Vreede, and F. van Rijs, "A compact 65 W 1.7–2.3 GHz class-E GaN power amplifier for base stations," in *Proc. 41st Eur. Microw. Conf.*, Oct. 2011, pp. 1103–1106.
[20] S. Rahimizadeh, J. Chéron, Q. Mu, and Z. Popović, "In-package harmonic termination design for improving active device efficiency," in *IEEE MTT-S Int. Microw. Symp. Dig.*, May 2016, pp. 1–4.
[21] D. A. Calvillo-Cortes, K. Shi, M. de Langen, F. van Rijs, and L. C. N. de Vreede, "On the design of package-integrated RF high-power amplifiers," in *IEEE MTT-S Int. Microw. Symp. Dig.*, Jun. 2012, pp. 1–3.
[22] G. Ahn *et al.*, "Design of a high-efficiency and high-power inverted Doherty amplifier," *IEEE Trans. Microw. Theory Techn.*, vol. 55, no. 6, pp. 1105–1111, Jun. 2007.
[23] J. H. Qureshi, W. Sneijers, R. Keenan, L. C. N. de Vreede, and F. van Rijs, "A 700-W peak ultra-wideband broadcast Doherty amplifier," in *IEEE MTT-S Int. Microw. Symp. Dig.*, Jun. 2014, pp. 1–4.
[24] J. H. Qureshi, W. Sneijers, and J. Gajadharsing, "Odd-mode Doherty power amplifier," in *IEEE MTT-S Int. Microw. Symp. Dig.*, May 2016, pp. 1–4.
[25] S. C. Cripps, *RF Power Amplifiers for Wireless Communication*. Norwood, MA, USA: Artech House, 2006.
[26] W. H. Doherty, "A new high-efficiency power amplifier for modulated waves," *Bell Syst. Tech. J.*, vol. 15, no. 3, pp. 469–475, Jul. 1936.
[27] J. He, J. H. Qureshi, W. Sneijers, D. A. Calvillo-Cortes, and L. C. N. de Vreede, "A wideband 700 W push-pull Doherty amplifier," in *IEEE MTT-S Int. Microw. Symp. Dig.*, May 2015, pp. 1–4.

[28] S. Afsardoost, T. Eriksson, and C. Fager, "Digital predistortion using a vector-switched model," *IEEE Trans. Microw. Theory Techn.*, vol. 60, no. 4, pp. 1166–1174, Apr. 2012.
[29] C. Huang, S. He, Z. Dai, J. Pang, and Z. Hu, "A 80 W high gain and broadband Doherty power amplifier for 4/5G wireless communication systems," in *IEEE MTT-S Int. Microw. Symp. Dig.*, May 2016, pp. 1–4.
[30] X. Chen, W. Chen, F. M. Ghannouchi, and Z. Feng, "A 1.1 GHz bandwidth, 46%-62% efficiency continuous mode Doherty power amplifier," in *IEEE MTT-S Int. Microw. Symp. Dig.*, May 2016, pp. 1–4.
[31] R. Giofré, L. Piazzon, P. Colantonio, and F. Giannini, "A distributed matching/combining network suitable for Doherty power amplifiers covering more than an octave frequency band," in *IEEE MTT-S Int. Microw. Symp. Dig.*, Jun. 2014, pp. 1–3.
[32] S. A. Bassam, F. M. Ghannouchi, and M. Helaoui, "2-D digital predistortion (2-D-DPD) architecture for concurrent dual-band transmitters," *IEEE Trans. Microw. Theory Techn.*, vol. 59, no. 10, pp. 2547–2553, Oct. 2011.
[33] X. Chen, W. Chen, Q. Zhang, F. M. Ghannouchi, and Z. Feng, "A 200 watt broadband continuous-mode Doherty power amplifier for base-station applications," in *IEEE MTT-S Int. Microw. Symp. Dig.*, Jun. 2017, pp. 1110–1113.
[34] S. Min, H. Christange, and M. Szymanowski, "Two-stage integrated Doherty power amplifier with extended instantaneous bandwidth for 4/5g wireless systems," in *IEEE MTT-S Int. Microw. Symp. Dig.*, Jun. 2017, pp. 122–125.
[35] X. A. Nghiem and R. Negra, "A 100 W GaN HEMT SPA-D with 57% fractional bandwidth for DVB-T applications," in *IEEE MTT-S Int. Microw. Symp. Dig.*, May 2016, pp. 1–4.
[36] X. Fang and K.-K. M. Cheng, "Broadband, wide efficiency range, Doherty Amplifier design using frequency-varying complex combining load," in *IEEE MTT-S Int. Microw. Symp. Dig.*, May 2015, pp. 1–4.
[37] D. Y.-T. Wu and S. Boumaiza, "A modified Doherty configuration for broadband amplification using symmetrical devices," *IEEE Trans. Microw. Theory Techn.*, vol. 60, no. 10, pp. 3201–3213, Oct. 2012.
[38] L. Piazzon, R. Giofrè, P. Colantonio, and F. Giannini, "A wideband Doherty architecture with 36% of fractional bandwidth," *IEEE Microw. Wireless Compon. Lett.*, vol. 23, no. 11, pp. 626–628, Nov. 2013.
[39] J. J. M. Rubio, V. Camarchia, M. Pirola, and R. Quaglia, "Design of an 87% fractional bandwidth Doherty power amplifier supported by a simplified bandwidth estimation method," *IEEE Trans. Microw. Theory Techn.*, vol. 66, no. 3, pp. 1319–1327, Mar. 2018.
[40] X. Chen, W. Chen, F. M. Ghannouchi, Z. Feng, and Y. Liu, "A broadband Doherty power amplifier based on continuous-mode technology," *IEEE Trans. Microw. Theory Techn.*, vol. 64, no. 12, pp. 4505–4517, Dec. 2016.
[41] J. Pang, S. He, C. Huang, Z. Dai, J. Peng, and F. You, "A post-matching Doherty power amplifier employing low-order impedance inverters for broadband applications," *IEEE Trans. Microw. Theory Techn.*, vol. 63, no. 12, pp. 4061–4071, Dec. 2015.

Abdul Raheem Qureshi (S'16) was born in Karachi, Pakistan, in 1984. He received the bachelor's degree (Hons.) in electronic engineering from the NED University of Engineering and Technology (UET), Karachi, in 2007, and the M.Sc. degree from Linkoping University, Linkoping, Sweden, in 2010. He is currently pursuing the Ph.D. degree at the Delft University of Technology, Delft, The Netherlands.

From 2010 to 2014, he was a Research Assistant with NED UET, where he was involved in various low-power CMOS power amplifier (PA) designs. From 2014 to 2015, he was a Ph.D. Intern with the NXP Semiconductors, Nijmegen, The Netherlands, where he was involved in high PAs design. In 2015, he joined Ampleon Netherlands B.V., Nijmegen, as a Ph.D. Intern. His current research interests include the area of RF PA design.

Mustafa Acar (S'04–M'07) received the B.S. degree (Hons.) from Middle East Technical University, Ankara, Turkey, in 2001, and the M.S. (Hons.) and Ph.D. degrees from the University of Twente, Enschede, The Netherlands, in 2003 and 2011, respectively.

From 2007 to 2015, he was with NXP Semiconductors, Nijmegen, The Netherlands, where he was involved in advanced RF power amplifier (PA) for base-station systems. From 2015 to 2017, he was with the Advanced Concepts and Systems Team, Ampleon Netherlands B.V., Nijmegen, where he was involved in massive multiple-in multiple-out (sub-6 GHz) high-efficiency PAs. He is currently with NXP Semiconductors, where he is involved in millimeter wave transmitters.

Sergio C. Pires (M'14) was born in Paris, France, in 1977. He received the degree in electrical engineering and Ph.D. degree from the University of Aveiro, Aveiro, Portugal, in 2000 and 2013, respectively.

From 2000 to 2002, he was an RF Network Planner with Optimus Telecommunications. From 2002 to 2007, he was an RF Systems Engineer with Chipidea Semiconductor, where he was involved in RF architectures, high-speed digital converters, and field applications systems. From 2007 to 2009, he was a Research and Development Department Leader for hardware development with Celfinet Telecommunications. From 2009 to 2014, he was a Researcher with the Telecommunications Institute, Aveiro, Portugal. From 2014 to 2015, he was a Senior Innovation Design Engineer with NXP Semiconductors, Nijmegen, The Netherlands. He is currently an Innovation Sr. Director with Ampleon Netherlands B.V., Nijmegen. His current research interests include highly efficient RF transmitter and RF transceiver architectures in both discrete and integrated circuits up to millimeter wave.

Dr. Pires has been a Reviewer for several journals, including the IEEE TRANSACTIONS ON MICROWAVE THEORY AND TECHNIQUES.

Leonardus Cornelis Nicolaas de Vreede (A'01–M'03–SM'04) received the Ph.D. degree (*cum laude*) from the Delft University of Technology, Delft, The Netherlands, in 1996.

In 1996, he was appointed as an Assistant Professor with the Delft University of Technology, where he was involved in the nonlinear distortion behavior of active devices with the Delft Institute of Microelectronics and Submicrometer Technology. From 1999 to 2015, he was appointed, respectively, an Associate Professor and a Full Professor with the Delft University of Technology, where he becomes responsible for the Electronic Research Laboratory, and involved in solutions for improved linearity and RF performance at the device, circuit, and system level. He is currently a co-founder/Advisor of Anteverta-mw, a company that specializes in RF device characterization. He has authored or co-authored over 130 IEEE refereed conference and journal papers. He holds several patents. His current research interest includes RF measurement systems, technology optimization, and energy-efficient/wideband circuit/system concepts for wireless applications.

Dr. de Vreede was a co-recipient of the IEEE Microwave Prize in 2008. He was a mentor of the Else Kooi Prize awarded Ph.D. work in 2010, and a mentor of the Dow Energy Dissertation Prize awarded Ph.D. work in 2011. He was a recipient of the TUD Entrepreneurial Scientist Award in 2015. He co-guided several students that won Best Paper Awards at BCTM, PRORISC, GAAS, ESSDERC, IMS, RFIT, and RFIC.